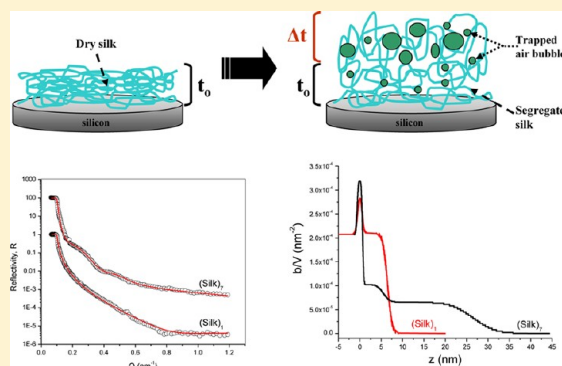


Silk Layering As Studied with Neutron Reflectivity

Brett Wallet,[†] Eugenia Kharlampieva,[†] Katie Campbell-Proszowska,[†] Veronika Kozlovskaya,[†] Sidney Malak,[†] John F. Ankner,[‡] David L. Kaplan,[§] and Vladimir V. Tsukruk^{*,†}[†]School of Materials Science and Engineering, Georgia Institute of Technology, Atlanta, Georgia 30332, United States[‡]Spallation Neutron Source, Oak Ridge National Laboratory, Oak Ridge, Tennessee 37831, United States[§]Department of Biomedical Engineering, Tufts University, Medford, Massachusetts 02155, United States

ABSTRACT: Neutron reflectivity (NR) measurements of ultrathin surface films (below 30 nm) composed of *Bombyx mori* silk fibroin protein in combination with atomic force microscopy and ellipsometry were used to reveal the internal structural organization in both dry and swollen states. Reconstituted aqueous silk solution deposited on a silicon substrate using the spin-assisted layer-by-layer (SA-LbL) technique resulted in a monolayer silk film composed of random nanofibrils with constant scattering length density (SLD). However, a vertically segregated ordering with two different regions has been observed in dry, thicker, seven-layer SA-LbL silk films. The vertical segregation of silk multilayer films indicates the presence of a different secondary structure of silk in direct contact with the silicon oxide surface (first 6 nm). The layered structure can be attributed to interfacial β -sheet crystallization and the formation of well-developed nanofibrillar nanoporous morphology for the initially deposited silk surface layers with the preservation of less dense, random coil secondary structure for the layers that follow. This segregated structure of solid silk films defines their complex nonuniform behavior in the D₂O environment with thicker silk films undergoing delamination during swelling. For a silk monolayer with an initial thickness of 6 nm, we observed the increase in the effective thickness by 60% combined with surprising decrease in density. Considering the nanoporous morphology of the hydrophobic silk layer, we suggested that the apparent increase in its thickness in liquid environment is caused by the air nanobubble trapping phenomenon at the liquid–solid interface.



The layered structure can be attributed to interfacial β -sheet crystallization and the formation of well-developed nanofibrillar nanoporous morphology for the initially deposited silk surface layers with the preservation of less dense, random coil secondary structure for the layers that follow. This segregated structure of solid silk films defines their complex nonuniform behavior in the D₂O environment with thicker silk films undergoing delamination during swelling. For a silk monolayer with an initial thickness of 6 nm, we observed the increase in the effective thickness by 60% combined with surprising decrease in density. Considering the nanoporous morphology of the hydrophobic silk layer, we suggested that the apparent increase in its thickness in liquid environment is caused by the air nanobubble trapping phenomenon at the liquid–solid interface.

INTRODUCTION

The control of the structural organization of proteins at interfaces with inorganic materials is crucially important for the design of bio-nanocomposite materials. Biology is full of examples in which material interfaces have been designed and assembled to provide unique properties, and strategies have been demonstrated to exhibit specific molecular control over these interfaces through self-assembly driven processes.^{1,2} Recently, silk fibroin protein has become an appealing biomaterial for implementation as a major component of hybrid biocomposites with applications ranging from sensing and optical systems to advanced structural composites.^{3–9} Several inherent physical properties suggest silk fibroin as a prospective candidate material in these areas including optical transparency, biocompatibility, biodegradability, and high strength combined with elasticity and mechanical robustness.^{10,11} The processing challenges in handling these high molecular weight proteins without aggregation has led to the use of reconstituted or regenerated silk fibroin aqueous solution for the fabrication of silk films and complex topological structures such as fibers and microcapsules.^{10,12–20} Production of silk fibroin solution for composite formation starts with the purification of harvested *Bombyx mori* cocoons by removing sericin, the glue-like binding component of silk. Sericin is a

water-soluble glycoprotein that binds fibroin filaments,¹ and although it contributes to increased mechanical properties of silk, it also has detrimental effects on the integration of silk into optical and biomedical devices.²¹

A balance of assorted forces including van der Waals, electrostatic, entropic, steric, hydrogen bonding, and hydrophobic interactions determines the secondary structure of silk molecules adsorbed at various interfaces.²² The unique properties of silk materials are caused by their order–disorder multidomain structure resulting from silk fibroin consisting of alternating hydrophobic and hydrophilic domains. Silk protein is rich in glycine and alanine residues, and the presence of GAGAS amino acid repeats are responsible for the formation of α -helices and β -sheet crystalline regions separated by random coil segments.²³ The transition between random coil conformation and silk crystalline ordering can be induced by changing solvent quality, drying conditions, and solvent treatments. Although the overall behavior of silk fibroin in solution and in bulk is fairly well understood, secondary silk structures at interfaces and close proximity to surfaces remain a

Received: March 3, 2012

Revised: June 10, 2012

Published: June 14, 2012

significant technical challenge. For example, the formation of helical structures at air–liquid interfaces as a polymorph of silk have been reported.^{24,25} These studies demonstrate that the crystalline structure, silk III, involves a left-handed, threefold helical chain conformation with hexagonal packing of silk molecules. Side chain character influences the stabilization of an interfacial conformation, suggesting that hydrophobic/hydrophilic interactions and partitioning drive the silk conformation at the air–liquid interface. However, information is still lacking regarding how increasing distance from the interface affects the silk chain conformation. Furthermore, the behavior of silk films in liquids, as well as their ability to swell after tethering to interfaces, remains uncharted.

In our recent study, we conducted ATR-FTIR of silk on silicon substrates and revealed that spin-assisted deposition immediately induced crystalline silk II formation from silk I structure (random coil conformation) in ultrathin films.¹¹ This transformation is believed to be facilitated via exposure of the ultrathin silk layer (~ 5 nm) to air in combination with shear forces, causing rapid dehydration of the film. In contrast, a relatively thick (~ 100 nm) dry spin-cast film displayed a predominantly random-coil structure under ambient conditions. The result is indicative of different structures pertaining to the ultrathin film versus the thicker one and the occurrence of significantly segregated interfacial structures. However, these studies provide only information on average conformation of silk molecules in particular films and cannot address the question of localized and propagating segregated phenomena and the effect of the interfacial confinement along the surface normal.

As is known, X-ray and neutron reflectivity techniques are capable of probing phenomena throughout thin films and revealing how interfacial interactions affect gradient of ordering along the surface normal^{26–29} with a spatial resolution at length scales ranging from submicrometers to that of intermolecular distances.³⁰ Several studies have been conducted using the combination of X-ray and neutron reflectivity techniques to investigate protein adsorption at interfaces,^{31–34} while various others focus solely on neutron reflectivity measurements to obtain desired adsorption information.^{35–38} Furthermore, neutron reflectivity has shown promising results for characterization of multilayer polymer films with inhomogeneous distribution of components.^{39–42}

However, most studies on silk fibroin have involved X-ray diffraction measurements of bulk materials to determine the structural characteristic of its three known conformations (random coil, silk I, and silk II) and do not provide insight into internal structuring of deposited silk layers.^{43–46} However, X-ray reflectivity does not provide the necessary contrast since the electron density contrast for biological systems is generally low,^{47–49} and the overall film microstructure composition is similar. On the other hand, neutron reflectivity examines length scales relevant for investigation of interactions of proteins and polymers, and adsorption of these molecules at liquid and solid surfaces.³⁰ An additional advantage of neutron reflectivity for this study is that the neutron scattering contrast between different isotopes of hydrogen, protium (^1H) and deuterium (^2H), can be exploited for examination of the swelling effect in ultrathin silk films. The high contrast of the absorption distribution across the interface is critical for obtaining rich structural information from nanostructured biopolymer–inorganic interfaces in the swollen state.⁵⁰ It is important to note that neutron reflectivity from silk swollen in contrasted

solvent is the only way to reveal any inhomogeneities related to interfacial reorganization in secondary structures such as β -sheet crystallization.

Thus, in the present communication, we report on neutron reflectivity studies conducted on ultrathin, molecular-level silk films (< 30 nm) in combination with atomic force microscopy imaging, spectroscopic ellipsometry studies, and previous FTIR data. Ultrathin films were fabricated using a reconstituted silk fibroin solution and spin-assisted layer-by-layer (LbL) assembly. Details regarding the interfacial behavior of silk macromolecules are revealed and depict a direct influence of the silicon oxide surface on structural organization within the films. We also demonstrate, via multiple silk layer deposition, the ability to tailor the structural density of these films by creating a silk template that becomes more dilute at the film–air interface at a certain distance from the substrate. In addition, the effect of swelling of the films with D_2O solvent is presented in order to provide information regarding film organization and stability at the solid–liquid interface.

■ EXPERIMENTAL SECTION

Reconstituted Silk Fibroin Solution. For all experiments, 18.2 $\text{M}\Omega\text{-cm}$ Nanopure water was utilized. Silk was obtained from *Bombyx mori* silkworms raised on a diet of Silkworm Chow (Mullberry Farms, Fallbrook, CA). Live pupae were extracted from the cocoons prior to sericin removal. Cocoons were boiled for 30 min in an aqueous solution of 0.02 M Na_2CO_3 and then rinsed thoroughly with distilled water to extract the glue-like sericin proteins. The extracted silk fibroin was then dissolved in 9.3 M LiBr solution at 60 °C for 4 h, yielding a 20% (w/v) solution. The solution was dialyzed against distilled water using Slide-a-Lyzer dialysis cassettes (Pierce, MWCO 3500) at room temperature for 3 days to remove the LiBr. After dialysis, the solution was centrifuged three times, each at 20 °C for 20 min, to remove impurities and the aggregates that occurred during dialysis. The final concentration of aqueous fibroin solution was 8.0% w/v, determined by weighing the remaining solid after drying. This solution was then diluted to obtain the desired 0.2% (w/v) silk concentration used for solution deposition.

Film Formation. Silk solution was spin coated on $\langle 100 \rangle$ silicon wafers with a diameter of 5 cm, thickness of 10 mm, and one polished side (purchased from the Institute of Electronic Materials Technology, Poland). A schematic demonstration of the deposition procedure is illustrated in Figure 1. The spin-assisted layer-by-layer (SA-LbL) deposition method was performed by sequentially dropping silk onto the silicon substrate using 3 mL shots of silk solution, rotating for 60 s at 3000 rpm on a spin-coater (Laurell Technologies), rinsing once with Nanopure water to remove unbound silk, followed by deposition of the next layer in accordance with usual procedure.⁶⁸ After film fabrication, the films were dried in ambient conditions for neutron reflectivity measurements. The LbL assembly method was used because it allows for the production of ultrathin films with greater control over thickness, composition, and properties at the nanometer-scale.^{51–55} We have already demonstrated the applicability of SA-LbL for designing robust and flexible ultrathin films with excellent mechanical properties.¹⁰ Furthermore, we have established the ability to fabricate similar films using the SA-LbL deposition approach in conjunction with reconstituted silk fibroin aqueous solution.^{11,13,56,57}

Film Characterization. The morphology of the pristine silk films was first characterized with a Dimension 3000 instrument (Digital Instruments) by conducting atomic force microscopy (AFM) imaging in the light tapping mode according to the established procedure using silicon tips with a cantilever spring constant of 50 N m^{-1} .^{58,59} Ellipsometry measurements of film thickness were performed with a Woollam M2000U multiangle spectroscopic ellipsometer with measurements at three different angles: 65°, 70°, and 75°. Thicknesses of dry films were determined using a data fit with the Cauchy model over the range of wavelengths, λ , of 250–1000 nm.

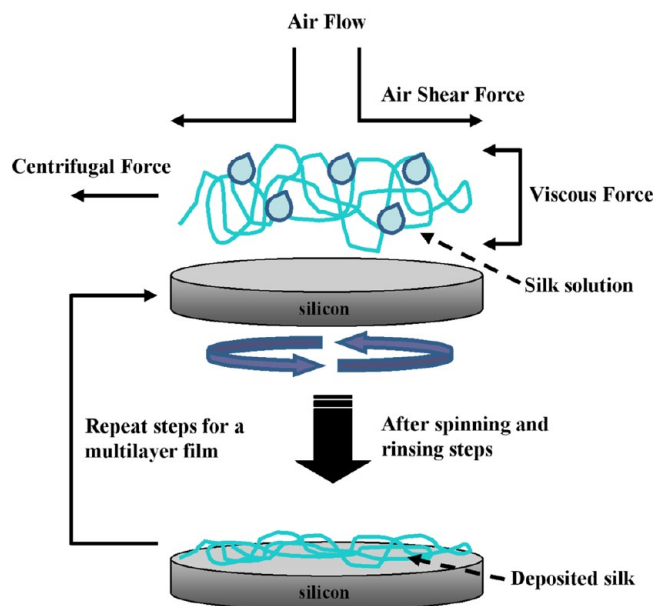


Figure 1. Schematic representation of the film assembly process.

Neutron Reflectivity. Neutron reflectivity measurements were conducted on dry and hydrated SA-LbL films at the Spallation Neutron Source Liquids Reflectometer (SNS-LR) at Oak Ridge National Lab (ORNL). The SNS-LR collects specular reflectivity data in a continuous-wavelength band at several different incident angles. Measurements were conducted in three independent series to ensure the reproducibility of the experimental data.

For the data presented here, we used the wavelength band of $0.2 \text{ nm} < \lambda < 0.55 \text{ nm}$ and measured reflectivity at angles of $\theta = 0.15, 0.25, 0.40, 0.75,$ and 1.20° , thereby spanning a wide total wavevector transfer range of $0.06 \text{ nm}^{-1} < Q < 1.2 \text{ nm}^{-1}$ where $Q = (4\pi \sin \theta)/\lambda$ where θ is the incident angle and λ is the neutron wavelength). The data were collected at each angle with incident-beam slits set to maintain the wavevector resolution constant at $\delta Q/Q = 0.05$, which allowed us to stitch the five different angle data sets together into a single reflectivity curve. We collected neutron reflectivity data from dry films as well as in a liquid environment by placing specimens in a liquid-cell with the top surface in contact with D_2O . Isotopic substitution of protium with deuterium, known as the contrast variation method, is frequently implemented due the large SLD contrast between the two when compared to hydrogen, thus enabling a clear distinction between structural inhomogeneities in the liquid state which cannot be otherwise revealed.^{39,41,45,61,67}

The data were analyzed using a model developed at ORNL with conventional NR data fitting techniques. To fit the experimental data, we started with an idealized film structure featuring sharp interfaces between adjacent layers. This model was then modified to accommodate the physically measured structures by adjusting layer thicknesses, scattering length density (SLD), and roughness to best model the measured data in both dry and swollen states.⁶⁰

Initial individual layer thicknesses for simulations were taken from ellipsometry measurements and then adjusted to the neutron reflectivity data. The neutron scattering density is defined as $\Sigma = b/V$, where b is the monomer scattering length (sum of the scattering lengths of constituent atomic nuclei) and V is the monomer volume.⁶⁰ The value of $(b/V)_n$ can be related to the molecular properties of the film through:

$$(b/V)_n = \frac{N_A \rho_b \sum b_i}{M_w} \quad (1)$$

where N_A is Avogadro's number, ρ_b is the mass density in the volume of interest, b_i is the scattering length of the i th element in the repeat

unit summed over all atoms in the repeat unit, and M_w is the molar mass of a representative repeat unit of the polymer.

Therefore, the SLD varies as a function of the mass density of the film as well as the local composition in the film.⁶¹ Standard SLD values were used for common materials including D_2O ($6.38 \times 10^{-6} \text{ \AA}^{-2}$) and silicon oxide ($3.76 \times 10^{-6} \text{ \AA}^{-2}$) unless otherwise noted. Layer intermixing was simulated by error function density profiles (Gaussian roughness).⁶² The swelling profile for $(\text{silk})_1$ was calculated as a ratio of all characteristic dimension points (e.g., midranges of transition zones and zones with constant SLD) in dry and in-fluid states as will be discussed below.

RESULTS AND DISCUSSION

Spectroscopic ellipsometry and AFM measurements were taken for independent verification of the film morphologies, roughness, and different layer thicknesses in the dry state (Table 1).

Table 1. Total Film Thicknesses and Microroughnesses (AFM and ellipsometry) for Dry and Swollen Silk Films

SA-LbL system	ellipsometry thickness (nm)	total film thickness by NR (nm)	AFM roughness (nm)
SiO_2	2.0	1.2	0.1
$(\text{silk})_1$ dry	4.4	6.0	3.2 ± 0.4
swollen	—	9.0	—
$(\text{silk})_7$ dry	27.8	31.0	2.4 ± 0.5
swollen	—	—	—

The film parameters determined from modeling the measured reflectivity data, thickness, SLD (N_b), and internal roughness (σ), are summarized in Table 2 with results discussed below.

Table 2. Neutron Reflectivity Model Parameters for Dry and Swollen Films

SA-LbL system	modeled film structure	$N_b \times 10^{-6}$ (nm^{-2})	d (nm)	roughness (nm)
SiO_2	SiO_2	376	1.2	0.5
$(\text{silk})_1$ dry	silk monolayer	210	6.0	2.0
$(\text{silk})_1$ swollen	dense silk (substrate)	185	5.5	0.9
	slightly swollen/expanded silk	110	3.5	2.5
	D_2O	638	—	—
$(\text{silk})_7$ dry	densely packed silk (substrate)	100	6.0	5.5
	loosely packed silk (air interface)	44	25.0	20.0

Dry Silk Films. AFM imaging of silk films in the dry state indicates relatively smooth, uniform surfaces over large areas without the presence of large microscale defects, a common feature of SA-LbL films from silk materials. Some nanofibrillar components with open porous morphology were visible for both silk films, a common feature for SA-LbL silk films.⁶³ Some larger-scale surface segregation becomes visible for thicker silk films, which may cause dissolution and delamination of the surface elements after long-term storage in liquid environments as will be discussed below.

At higher magnification, the characteristic fine domain texture was observed with domain dimensions below 50 nm, which are organized into elements of nanofibrillar structures as has been observed and discussed for ultrathin silk films earlier (Figure 2).^{63,64} The domains are smaller in the thicker film and show a higher tendency to form random nanofibrillar structures

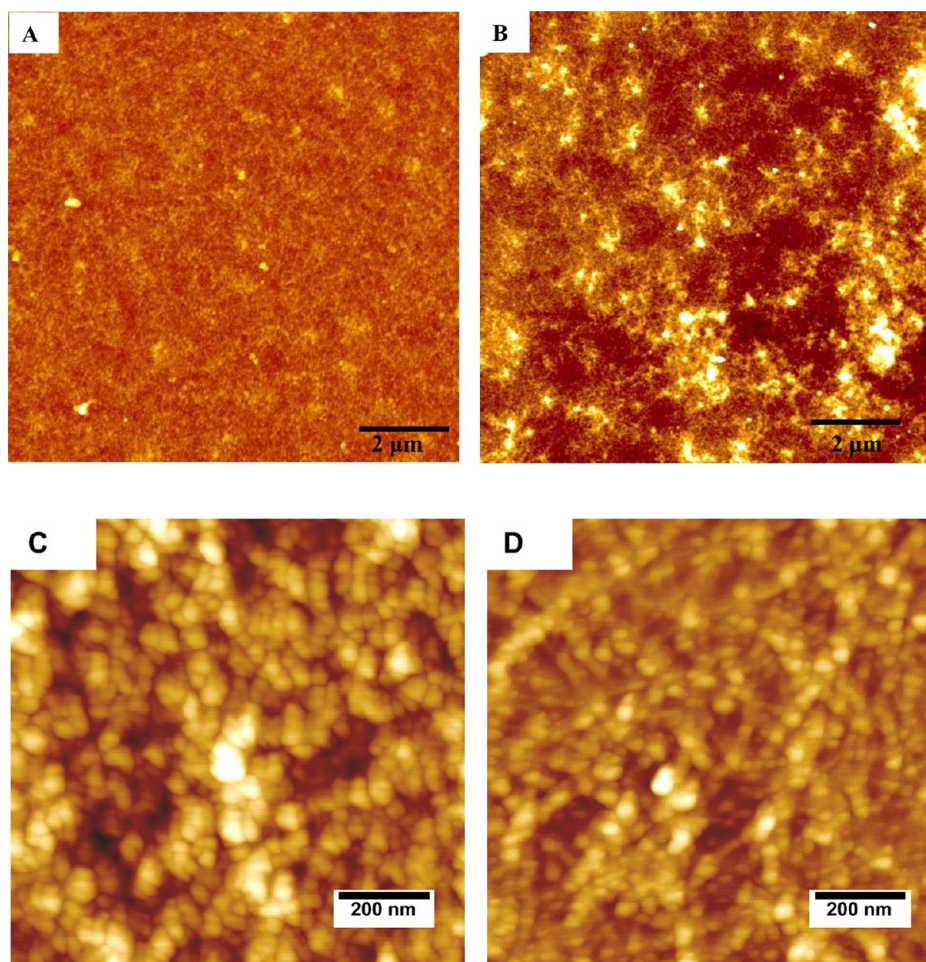


Figure 2. Topographical AFM images at different scales of (a, c) $(\text{silk})_1$ monolayer and (b, d) $(\text{silk})_7$ multilayer films.

and highly porous morphology. This is likely caused by the longer exposure to wet conditions during multiple depositions which promotes the formation of nanofibrillar structures at hydroxyl-terminated silicon oxide surfaces.⁶³ A distinct feature of both surfaces is extremely high porosity with pore sizes below 50 nm and high estimated surface coverage which can easily reach 50% for the topmost layer.

The surface microroughness of the silk films calculated over a $1 \times 1 \mu\text{m}^2$ surface area resulted in similar values of 3.2 ± 0.4 nm and 2.4 ± 0.5 nm for the $(\text{silk})_1$ and $(\text{silk})_7$ films, respectively, reflecting the similarity of the domain texture of the topmost silk layer. Through modeling of the neutron reflectivity data, the global surface roughness can be determined for comparison to AFM data by using the σ value associated with the modeled layer nearest the air interface (Tables 1, 2). The external roughness values obtained from neutron reflectivity increase to 20 nm for dry $(\text{silk})_7$ films, reflecting a rough and diffuse surface for thicker films with segregated surface nanofibrils, open pores, and domains across the whole silicon wafer.

Before neutron reflectivity measurements, the film thicknesses were measured with ellipsometry (Table 1). These thicknesses [$(\text{silk})_1 = 4.4$ nm and $(\text{silk})_7 = 27.8$ nm] corresponded well to those reported in earlier results.¹⁰ The following neutron reflectivity models provide similar but slightly larger thickness values, $(\text{silk})_1 = 6.0$ nm and $(\text{silk})_7 = 31.0$ nm, reflecting the overall uniformity of the silk films as

probed with very different wavelengths (Tables 1, 2). For simplicity, we refer to these films below as thin and thick for $(\text{silk})_1$ and $(\text{silk})_7$ films, respectively.

In Figure 3, $\log R$ is plotted as a function of momentum transfer, Q . For both silk films there were no distinct Bragg

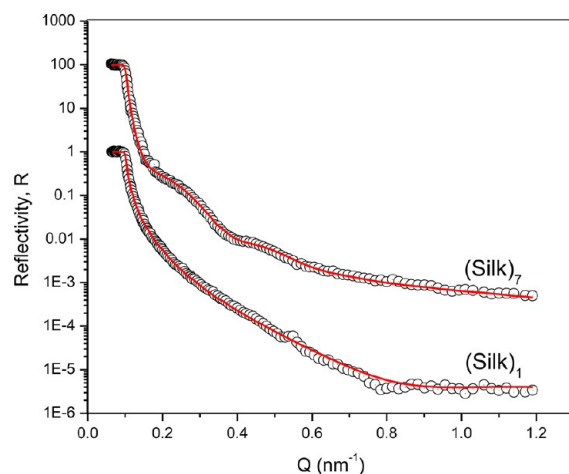


Figure 3. Neutron reflectivity data for dry $(\text{silk})_1$ and $(\text{silk})_7$ films where symbols and solid lines in the plot represent the experimental data and fit, respectively. The $(\text{silk})_7$ curve is displaced vertically by a factor of 100 for clarity.

peaks present indicating an absence of periodic stratification.^{65–67} Critical Q values were similar for both films and the overall shape in mid- Q range can be used to model the overall film thickness as well as the internal vertical distribution for silk films. The fitting enabled minimum deviations between the modeled reflectivity profile and the measured data (see experimental data points along with solid fitting curves (Figure 3)).

The scattering length density profiles obtained from the fitting procedure show the density distribution (SLD) along the direction normal to the film surface (Figure 4). The SLD

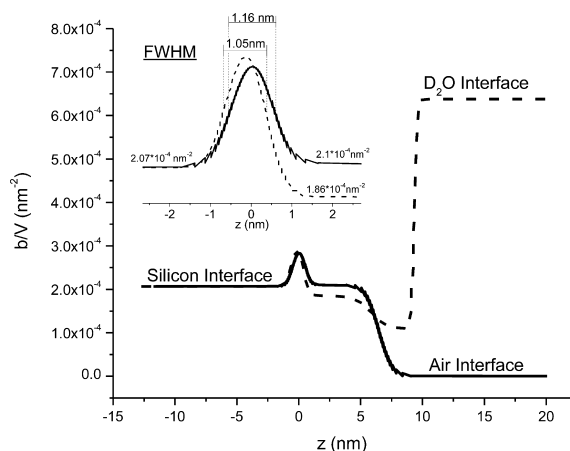


Figure 4. Neutron SLD profiles for (silk)₁ in both dry (solid) and swollen (dashed) states. Inset shows profile at the silicon-dioxide–silk interface.

profile for the dry (silk)₁ monolayer indicates that a single, relatively dense and probably partially crystalline silk monolayer (see below) of 6 nm thickness forms on the silicon oxide surface under these spin-cast deposition conditions. The interface between the silicon oxide layer and the silk film was determined to be relatively smooth, with roughness less than 1 nm. The roughness of the silk film itself was determined to be 2.0 nm, in good agreement with the AFM experimental data (Tables 1, 2).

It is well-known that the driving force for the assembly of silk fibroin in a layered manner is related to hydrophobic, ionic, and hydrogen bonding interactions.⁶⁸ The interface formed between silk molecules and surface hydroxyl groups on the silicon substrate acts to form and stabilize nanofibril bundles formed by silk backbones in β -sheet conformation via minimization of interaction of these hydrophobic domains with highly hydrophilic surface.^{25,69,70} Sequential hydrophobic and hydrophilic blocks are thus an important design feature for the assembly of silk at interfaces.^{71,72} Extensive hydrophobic glycine-alanine repeats with tyrosine present facilitate hydrophobic interactions and dewetting of β -sheet domains in wet environments and thus intense formation of organized nanofibrillar structures in close proximity to the silicon surface.^{71,73,74} On the other hand, the extensive hydrogen bonding of amino acids (such as glycine, alanine, and serine) stabilize the overall morphology of silk surface layer.^{70,75}

Indeed, as has been already demonstrated by detailed FTIR studies on mono- and multilayered silk films, the dehydration of the silk surface layer during the spin-casting promotes hydrogen-bonding and β -sheet formation.^{11,64,68,74} These FTIR results on the secondary structure of dry silk monolayers indicated

conversion of silk layers to the crystalline β -sheet silk II structure with higher density as well as preservation of nonorganized, random coil silk in thicker films with β -sheet content reaching 40–50%. Therefore, we suggest that the silk monolayer is predominantly composed of denser silk in a β -sheet secondary structure as segregated nanofibrils and pores.

The modeling of the reflectivity data for the thicker (silk)₇ film indicates a much more complex internal film structure, requiring a two-component model to account for drastically different scattering at the silicon-silk interface versus the air-silk interface (Figure 5). In this case, the SLD profile obtained from

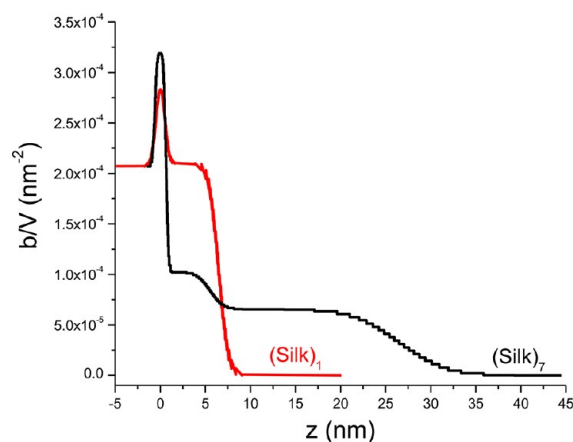


Figure 5. Neutron SLD profiles for (silk)₇ in the dry state. Data for swollen film is not presented. As discussed in the text, a large portion of the swollen (silk)₇ film are delaminated, resulting in an extremely rough film and reflectivity curve that could not be modeled.

the best fit is composed of two layers with a thin (6 nm) layer with higher SLD level at the silicon-silk interface and a more loosely packed and much thicker (25 nm) topmost silk layer with lower SLD (Figure 5).

The presence of two distinct regions of low and high densities indicates different secondary structures of thicker silk films. The thickness of the higher SLD region of about 6 nm coincides with the thickness of the monolayer silk, although the SLD is lower by about half compared to that determined for the dry (silk)₁ monolayer, and therefore, the (silk)₇ interfacial layer is much less dense. This density reduction can be directly related to highly porous inner microstructure and a stronger tendency to form nanofibrillar structures resulting in higher porosity after multiple wet depositions as revealed by AFM (see above). Large scale surface segregation and probably partial removal of the topmost silk material during consequential deposition and washing cycles facilitate much lower density of the thick (25 nm) topmost layer.

Swollen Silk Films. The reflectivity curves for both (silk)₁ and (silk)₇ films swollen in D₂O become smeared in the swollen-state when compared to the dry state (Figure 6). The effects of swelling are most apparent in the case of the (silk)₁ films, particularly when comparing the SLD profiles of dry silk to swollen (silk)₁ as shown in Figure 4. Overall, the (silk)₁ film exhibited dramatic expansion with swelling ratio of about 1.6 after immersion in D₂O with the nonuniform SLD distribution. It might be expected that diffusion of D₂O within the silk layers causes an increase in apparent density for those layers relative to a loosely packed region in the dry (silk)₇ film. It is worth noting that no signs of increased SLD level were observed, which can be associated with H-D exchange.

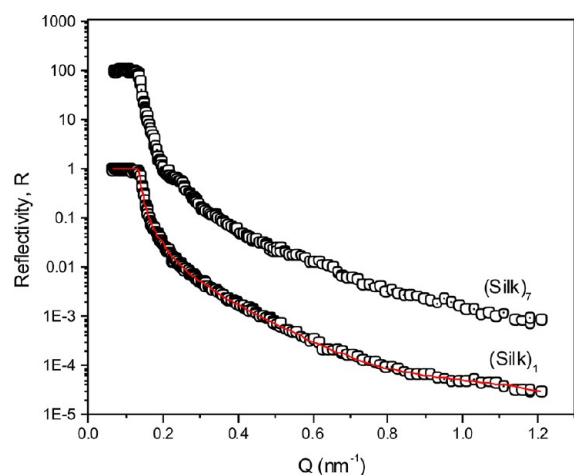


Figure 6. Neutron reflectivity data for (silk)₁ (open circles) and (silk)₇ (filled circles) films in D₂O medium where symbols and solid lines in the plot represent the experimental data and fit, respectively. Modeled reflectivity curve is only presented in the case of swollen (silk)₁ because of delamination of thicker film in swollen state. The (silk)₇ curve is displaced vertically by a factor of 10² for clarity.

However, surprisingly, an interfacial region of approximately 5 nm (in the vicinity of silicon oxide surface) remains virtually unswollen and densely packed, as indicated by an SLD that is only slightly lower than that of the dry (silk)₁ monolayer probably. The SLD did not increase drastically as would be expected for swelling and uptake of D₂O, which is in agreement with the fact that this interfacial region is composed of the porous morphology with a network of hydrophobic nanofibrillar structures. The contact angle of silk surface of about 70° corresponds to hydrophobic surface and open porous morphology is favorable for the formation of air nanobubbles at the liquid–solid interface.^{76,77} We can speculate that air nanobubbles can be trapped in the region in open nanopores which prevents the penetration of liquid into the highly porous morphology with the network of nanofibrillar hydrophobic asperities similar to those observed for porous hydrophobic synthetic and biological surfaces in different fluid environments.⁷⁸ The presence of trapped air bubbles should lead to increased porosity and the reduction of the effective density of the silk layer after immersion in liquid environment.

To quantify this nonuniform expansion, we calculated the “swelling ratio” profiles for the (silk)₁ film to reflect the local change in linear expansion of specific structural elements within silk monolayers (Figure 7). Similar calculations were not performed for the swollen (silk)₇ film due to the loss of silk material into the D₂O swelling medium during measurement and the inability to quantitatively describe the film using an SLD profile.

The swelling profile of the monolayer silk film confirms highly nonuniform swelling and the formation of distinct two-tier swollen structures for the silk monolayers (Figure 7). The swelling profile has been calculated by direct comparison of thickness which can be assigned to different characteristic elements of the SLD profile: onset of SLD plateau, midpoint of the SLD plateau, onset of the transition region, midpoint of transition region, and the film surface. As this analysis shows, a fraction of the interfacial monolayer retains virtually unchanged and the apparent swelling ratio remains close to 1.0 (Figure 7).

Then, the upper fraction of the monolayer becomes expanded by about 60%, forming the more loosely packed

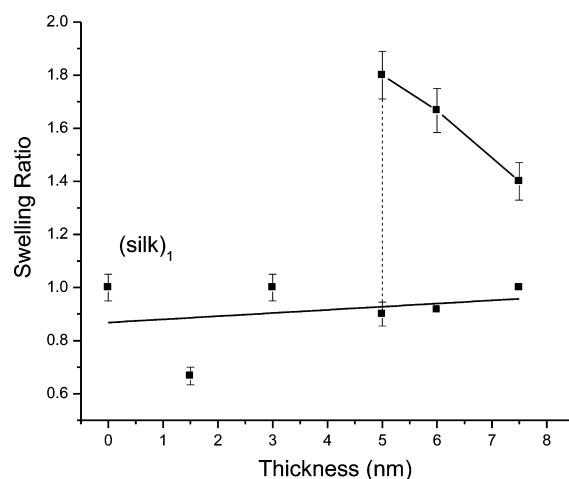


Figure 7. “Swelling ratio” profile for (silk)₁ film as determined by comparing SLD profiles in dry and wet states. Each data point represents ratio of expanded/initial thicknesses for characteristic points in the profile (see text).

nanofibrillar structures with relatively limited water intrusion in this hydrophobic region due to trapped bubbles as suggested above (Figure 8). Such a surprising finding reveals that even a single monolayer of solid silk material which is partially transformed into the silk II phase in segregated nanofibrillar structures in the vicinity of the silicon surface can be *expanded due to trapped air bubbles but are not per se highly swollen* after addition of liquid.

In the case of (silk)₇ films, the analysis is significantly more complicated. As shown in the reflectivity curve for the multilayer film in D₂O, the reflectivity does not go to 1 below the critical edge (Q_c) but instead slopes downward steeply in Q (Figure 6). This is signature of an extremely rough surface that cannot be treated with the optical model used to model reflectivity data for uniform films. The highly rough surface is likely formed due to a large portion of the silk films and surface aggregates delaminating during measurements which has also also confirmed with AFM measurements (not shown).

CONCLUSIONS

In conclusion, the neutron reflectivity studies conducted here have focused on (1) the depth profile of the layer organization within SA-LbL films as a function of film thickness and (2) the effect of swelling within the silk film structure as measured in situ. Under dry state conditions, the multilayer film resulted in a complex internal structure with two separate regions of SLD representing a denser microstructure near the SiO₂–silk interface brought on by the chosen deposition process and the formation of nanofibrillar morphologies. The surface-initiated segregation to the substrate (within the first 6 nm) can be associated with the interfacial crystallization in the β -sheet domains and nanofibrillation, with less dense random morphologies far from the interface.

Such a vertically segregated structure of solid silk films, which can be described by a two-layered model, explains their complex nonuniform swelling behavior in the presence of water. In the case of silk monolayers, the nonuniform swelling resulted in the formation of a two-tier expanded layer with a highly segregated and completely surface layer below 6 nm with trapped air bubbles. The expanded topmost layer is composed

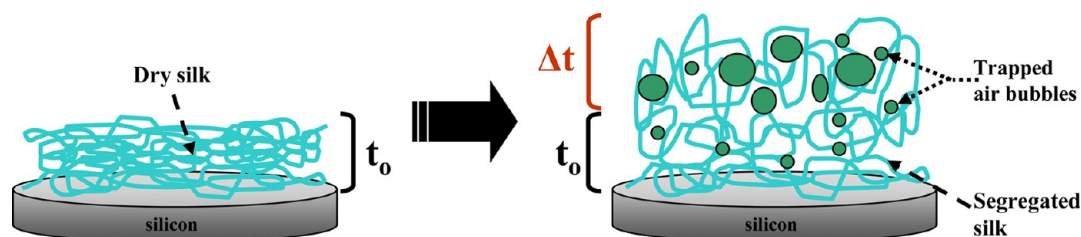


Figure 8. Two-tier swollen morphology of ultrathin silk films where the t_0 region indicates mostly interfacial segregated silk II nanofibrils and air nanobubbles, and Δt_1 represent the expanded region of expanded random silk and trapped air bubbles.

of random silk with trapped air bubbles with the integrated swelling ratio of the initial layer reaching 1.6. These studies indicate complex layering of silk in contact with silicon oxide surfaces in both dry and hydrated environments which have never observed in earlier studies and can be critical for processing and design of silk-filler interfaces in composite biomaterials.

AUTHOR INFORMATION

Notes

The authors declare no competing financial interest.

ACKNOWLEDGMENTS

This material is based upon work supported by the Air Force Office of Scientific Research under AFOSR-FA9550-08-1-0446, FA9550-10-1-0172, FA9550-09-1-0513 Grants (silk film formation) and Department of Energy Award DE-FG02-09ER46604 (neutron studies). Research at Oak Ridge National Laboratory's Spallation Neutron Source was sponsored by the Scientific User Facilities Division, Office of Basic Energy Sciences, U.S. DOE.

REFERENCES

- (1) Buehler, M. J.; Yung, Y. C. Deformation and Failure of Protein Materials in Physiologically Extreme Conditions and Disease. *Nat. Mater.* **2009**, *8*, 175.
- (2) Lawrence, B. D.; Cronin-Golomb, M.; Georgakoudi, I.; Kaplan, D. L.; Omenetto, F. G. Bioactive Silk Protein Biomaterial Systems for Optical Devices. *Biomacromolecules* **2008**, *9*, 1214.
- (3) Perry, H.; Gopinath, A.; Kaplan, D. L.; Dal Negro, L.; Omenetto, F. G. Nano- and Micropatterning of Optically Transparent, Mechanically Robust, Biocompatible Silk Fibroin Films. *Adv. Mater.* **2008**, *20*, 3070.
- (4) Amsden, J. J.; Perry, H.; Boriskina, S. V.; Gopinath, A.; Kaplan, D. K.; Dal Negro, L.; Omenetto, F. G. Spectral analysis of Induced Color Change on Periodically Nanopatterned Silk Films. *Opt. Express* **2009**, *17*, 21271.
- (5) Liu, Y.; Liu, H.; Qian, J.; Deng, J.; Yu, T. Entrapment of both Glucose Oxidase and Peroxidase in Regenerated Silk Fibroin Membrane. *Fresenius' J. Anal. Chem.* **1996**, *355*, 78.
- (6) Yu, T.; Liu, H.; Deng, J.; Liu, Y. Characterization of Regenerated Silk Fibroin Membranes for Immobilizing Glucose Oxidase and Construction of a Tetrathiafulvalene-mediated Glucose Sensor. *J. Appl. Polym. Sci.* **1995**, *58*, 973.
- (7) Zhang, Y.-Q. Natural Silk Fibroin as a Support for Enzyme Immobilization. *Biotechnol. Adv.* **1998**, *16*, 961.
- (8) Vepari, C.; Kaplan, D. K. Silk as a Biomaterial. *Prog. Polym. Sci.* **2007**, *32*, 991.
- (9) Kearns, V.; MacIntosh, A. C.; Crawfords, A.; Hatton, P. V. Silk-based Biomaterials for Tissue Engineering. In *Topics in Tissue Engineering*; Ashammakhi, N., Reis, R., Chiellini, F., Eds.; 2008; Vol. 4.
- (10) Jiang, C.; Wang, X.; Gunawidjaja, R.; Lin, Y.-H.; Gupta, M. K.; Kaplan, D. L.; Naik, R. R.; Tsukruk, V. T. Mechanical Properties of Robust Ultrathin Silk Fibroin Films. *Adv. Funct. Mater.* **2007**, *17*, 2229.

(11) Kharlampieva, E.; Zimnitsky, D.; Gupta, M.; Bergman, K. N.; Kaplan, D. L.; Naik, R. R.; Tsukruk, V. T. Redox-Active Ultrathin Template of Silk Fibroin: Effect of Secondary Structure on Gold Nanoparticle Reduction. *Chem. Mater.* **2009**, *21*, 2696.

(12) Kharlampieva, E.; Tsukruk, T.; Slocik, J. M.; Ko, H.; Poulsen, N.; Naik, R. R.; Kroger, N.; Tsukruk, V. T. Bioenabled Surface-Mediated Growth of Titania Nanoparticles. *Adv. Mater.* **2008**, *22*, 3274.

(13) Shchepelina, O.; Drachuk, I.; Gupta, M. K.; Lin, J.; Tsukruk, V. V. Silk-on-Silk LbL Microcapsules. *Adv. Mater.* **2011**, *23*, 4655.

(14) Martel, A.; Burghammer, M.; Davies, R. J.; Cola, E. D.; Vendrely, C.; Riekel, C. J. Silk Fiber Assembly Studied by Synchrotron Radiation SAXS/WAXS and Raman Spectroscopy. *J. Am. Chem. Soc.* **2008**, *130*, 17070.

(15) Jin, H.; Kaplan, D. Mechanism of Silk Processing in Insects and Spiders. *Nature* **2003**, *424*, 1057.

(16) Zhu, J.; Zhang, Y.; Shao, H.; Hu, X. Electrospinning and Rheology of Regenerated Bombyx Mori Silk Fibroin Aqueous Solutions: The Effects of pH and Concentration. *Polymer* **2008**, *49*, 2880.

(17) Chen, X.; Shao, Z.; Knight, D.; Vollrath, F. Conformation Transition Kinetics of Bombyx Mori Silk Protein. *Proteins: Struct., Funct., Bioinf.* **2007**, *68*, 223.

(18) Martel, A.; Burghammer, M.; Davies, R.; Cola, R. D. A Microfluidic Cell for Studying the Formation of Regenerated Silk by Synchrotron Radiation Small- and Wide-angle X-ray Scattering. *Biomicrofluidics* **2008**, *2*, 024104.

(19) Zhu, Z. H.; Ohgo, K.; Asakura, T. Preparation and Characterization of Regenerated Bombyx Mori Silk Fibroin Fiber with High Strength. *eXPRESS Polym. Lett.* **2008**, *2*, 885.

(20) Ye, C.; Shchepelina, O.; Calabrese, R.; Drachuk, I.; Kaplan, D. L.; Tsukruk, V. V. Robust and Responsive Silk Ionomer Microcapsules. *Biomacromolecules* **2011**, *12*, 4319.

(21) Meinel, L.; Hofmann, S.; Karageorgiou, V.; Kirker-Head, C.; McCool, J.; Gronowicz, G.; Zichner, L.; Langer, R.; Vunjak-Novakovic, G.; Kaplan, D. K. The Inflammatory Responses to Silk Films in vitro and in vivo. *Biomaterials* **2005**, *26*, 147.

(22) Yano, Y. F.; Uruga, T.; Tanida, H.; Terada, Y.; Takagaki, M.; Yamada, H. Driving Force Behind Adsorption-Induced Protein Unfolding: A Time-Resolved X-ray Reflectivity Study on Lysozyme Adsorbed at an Air/Water Interface. *Langmuir* **2009**, *25*, 32.

(23) Xu, M.; Lewis, R. V. Structure of a Protein Superfiber: Spider Dragline Silk. *Proc. Natl. Acad. Sci. U.S.A.* **1990**, *87*, 7120.

(24) Valluzzi, R.; Gido, S. P.; Muller, W.; Kaplan, D. L. Enzymatic Degradation Properties of Silk Fibroin Film. *Int. J. Biol. Macromol.* **1999**, *24*, 237.

(25) Valluzzi, R.; He, S. J.; Gido, S. P.; Kaplan, D. Bombyx Mori Silk Fibroin Liquid Crystallinity and Crystallization at Aqueous Fibroin-organic Solvent Interfaces. *Int. J. Biol. Macromol.* **1999**, *24*, 227.

(26) Dailant, J.; Gibaud, A. *X-ray and Neutron Reflectivity: Principles and Applications*; Springer: Berlin, 1999.

(27) Tolan, M. *X-ray Scattering from Soft Matter Thin Films*; Springer: Berlin, 1999.

(28) Foster, M. D. X-Ray Scattering Methods for the Study of Polymer Interfaces. *Crit. Rev. Anal. Chem.* **1993**, *24*, 179.

- (29) Peri, S.; Akgun, B.; Satija, S. K.; Jiang, H.; Enlow, J.; Bunning, T.; Foster, M. Control of Interface Nanoscale Structure Created by Plasma-Enhanced Chemical Vapor Deposition. *ACS Appl. Mater. Interfaces* **2011**, *3*, 3375.
- (30) Harroun, T. A.; Kucerka, N.; Nieh, M.-P.; Katsaras. Neutron and X-ray Scattering for Biophysics and Biotechnology: Examples of Self-Assembled Lipid Systems. *Soft Matter* **2009**, *5*, 2694.
- (31) Vaknin, D.; Kjaer, K.; Ringsdorf, H.; Blankenburg, R.; Piepenstock, M.; Diedrich, A.; Losche, M. X-Ray and Neutron Reflectivity Studies of a Protein Monolayer Adsorbed to a Functionalized Aqueous Surface. *Langmuir* **1993**, *9*, 1171.
- (32) Yano, Y. F.; Uruga, T.; Tanida, H.; Terada, Y.; Takagaki, M.; Yamada, H. Driving Force Behind Adsorption-Induced Protein Unfolding: A Time-Resolved X-ray Reflectivity Study on Lysozyme Adsorbed at an Air/Water Interface. *Langmuir* **2009**, *25*, 32.
- (33) Evers, F.; Shokuie, K.; Paulus, M.; Sternemann, C.; Czeslik, C.; Tolan, M. Exploring the Interfacial Structure of Protein Adsorbates and the Kinetics of Protein Adsorption: An in situ High-Energy X-ray Reflectivity Study. *Langmuir* **2008**, *24*, 10216.
- (34) Sheller, N. B.; Petrash, S.; Foster, M. D.; Tsukruk, V. V.; X-ray, A. F. M. Reflectivity Studies of Albumin Adsorbed onto Self-Assembled Monolayers. *Langmuir* **1998**, *14*, 4535.
- (35) Green, R. J.; Su, T. J.; Lu, J. R.; Webster, J. R. P. The Displacement of Preadsorbed Protein with a Cationic Surfactant at the Hydrophilic SiO₂-water Interface. *J. Phys. Chem. B* **2001**, *105*, 9331.
- (36) Kent, M. S.; Yim, H.; Sasaki, D. Y. Adsorption of Myoglobin to Cu(II)-IDA and Ni(II)-IDA Functionalized Langmuir Monolayers: Study of the Protein Layer Structure During the Adsorption Process by Neutron and X-ray Reflectivity. *Langmuir* **2005**, *21*, 6815.
- (37) Evers, F.; Steitz, R.; Tolan, M.; Czeslik, C. Analysis of Hofmeister Effects on the Density Profile of Protein Adsorbates: A Neutron Reflectivity Study. *J. Phys. Chem. B* **2009**, *113*, 8462.
- (38) Haas, H.; Steitz, R.; Fasano, A.; Liuzzi, G. M.; Polverini, E.; Cavatorta, P.; Riccio, P. Laminar Order within Langmuir-Blodgett Multilayers from Phospholipid and Myelin Basic Protein: A Neutron Reflectivity Study. *Langmuir* **2007**, *23*, 8491.
- (39) Jean, B.; Dubreuil, F.; Heux, L.; Cousin, F. Structural Details of Cellulose Nanocrystals/Polyelectrolytes Multilayers Probed by Neutron Reflectivity and AFM. *Langmuir* **2008**, *24*, 3452.
- (40) Losche, M.; Schmitt, J.; Decher, G.; Bouwman, W. G.; Kjaer, K. Detailed Structure of Molecularly Thin Polyelectrolyte Multilayer Films on Solid Substrates as Revealed by Neutron Reflectometry. *Macromolecules* **1998**, *31*, 8893.
- (41) Russell, T. P.; Karim, A.; Mansour, A.; Felcher, G. P. Specular Reflectivity of Neutrons by Thin Polymer Films. *Macromolecules* **1988**, *21*, 1890.
- (42) Dufresne, A. Processing of Polymer Nanocomposites Reinforced with Polysaccharide Nanocrystals. *Molecules* **2010**, *15*, 4111.
- (43) Marsh, R. E.; Corey, R. B.; Pauling, L. An Investigation of the Structure of Silk Fibroin. *Biochim. Biophys. Acta* **1955**, *16*, 1.
- (44) Takahashi, Y.; Gehoh, M.; Yuzuriha, K. Crystal-Structure of Silk (Mombyx-Mori). *J. Polym. Sci., Part B: Polym. Phys.* **1991**, *29*, 889.
- (45) Lotz, B.; Keith, H. D. Crystal Structure of Poly(L-ALA-GLY)II – Model for Silk I. *J. Mol. Biol.* **1971**, *61*, 201.
- (46) Saitoh, H.; Ohshima, K.-I.; Tsubouchi, K.; Takasu, Y.; Yamada, H. X-ray Structural Study of Noncrystalline Regenerated Bombyx Mori Silk Fibroin. *Int. J. Biol. Macromol.* **2004**, *34*, 259.
- (47) Paulus, M.; Lietz, D.; Sternemann, C.; Shokuie, K.; Evers, F.; Tolan, M.; Czeslik, C.; Winter, R. J. An Access to Buried Interfaces: The X-ray Reflectivity Set-up at DELTA. *J. Synchrotron Radiat.* **2008**, *15*, 600.
- (48) Seeck, O. H.; Kaendler, I. D.; Tolan, M.; Shin, K.; Rafailovich, M. H.; Sokolov, J.; Kolb, R. Analysis of X-ray Reflectivity Data from Low-Contrast Polymer Bilayer Systems Using a Fourier Method. *Appl. Phys. Lett.* **2000**, *76*, 2713.
- (49) Fragneto-Cusani, G. Neutron Reflectivity at the Solid/Liquid Interface: Examples of Applications in Biophysics. *J. Phys.: Condens. Matter* **2001**, *13*, 4973.
- (50) Cullity, B. D. *Elements of X-Ray Diffraction*, second ed.; Addison Wesley: 1978.
- (51) *Multilayer Thin Films: Sequential Assembly of Nanocomposite Materials*; Decher, G., Schlenoff, J. B., Eds.; Wiley-VCH: Weinheim, 2002.
- (52) Hiller, J. A.; Mendelsohn, J. D.; Rubner, M. F. Reversibly Erasable Nanoporous Anti-Reflection Coatings from Polyelectrolyte Multilayers. *Nat. Mater.* **2002**, *1*, 59.
- (53) Schlenoff, J. B.; Rmaile, A. H.; Bucur, C. B. Hydration Contributions to Association in Polyelectrolyte Multilayers and Complexes: Visualizing Hydrophobicity. *J. Am. Chem. Soc.* **2008**, *130*, 13589.
- (54) Lvov, Y.; Decher, G.; Möhwald, H. Assembly, Structural Characterization, and Thermal-Behavior of Layer-by-Layer Deposited Ultrathin Films of Poly(Vinyl Sulfate) and Poly(Allylamine). *Langmuir* **1993**, *9*, 481.
- (55) Lvov, Y.; Ariga, K.; Ichinose, I.; Kunitake, T. Formation of Ultrathin Multilayer and Hydrated Gel from Montmorillonite and Linear Polycations. *Langmuir* **1996**, *12*, 3038.
- (56) Kharlampieva, E.; Kozlovskaya, V.; Gunawidjaja, R.; Shevchenko, V. V.; Vaia, R.; Naik, R. R.; Kaplan, D. L.; Tsukruk, V. V. Flexible Silk-Inorganic Nanocomposites: From Transparent to Highly Reflective. *Adv. Funct. Mater.* **2010**, *20*, 840.
- (57) Kharlampieva, E.; Kozlovskaya, V.; Wallet, B.; Shevchenko, V. V.; Naik, R. R.; Vaia, R.; Kaplan, D. L.; Tsukruk, V. V. Co-crosslinking silk matrices with silica nanostructures for robust ultrathin nanocomposites. *ACS Nano* **2010**, *4*, 7053.
- (58) Tsukruk, V. V. Scanning Probe Microscopy of Polymer Surfaces. *Rubber Chem. Technol.* **1997**, *70*, 430.
- (59) McConney, M. E.; Singamaneni, S.; Tsukruk, V. V. Probing Soft Matter with the Atomic Force Microscopies: Imaging and Force Spectroscopy. *Polym. Rev.* **2010**, *50*, 235.
- (60) Kharlampieva, E.; Kozlovskaya, V.; Chan, J.; Ankner, J. F.; Tsukruk, V. V. Spin-Assisted Layer-by-Layer Assembly: Variation of Stratification as Studied with Neutron Reflectivity. *Langmuir* **2009**, *25*, 14017.
- (61) Peri, S. R.; Habersberger, B.; Akgun, B.; Jiang, H.; Enlow, J.; Bunning, T. J.; Majkrzak, C. F.; Foster, M. D. Variations in Cross-link Density with Deposition Pressure in Ultrathin Plasma Polymerized Benzene and Octafluorocyclobutane Films. *Polymer* **2010**, *51*, 4390.
- (62) Jomaa, H. W.; Schlenoff, J. B. Salt-Induced Polyelectrolyte Interdiffusion in Multilayered Films: A Neutron Reflectivity Study. *Macromolecules* **2005**, *38*, 8473.
- (63) Shulha, H.; Wong, C.; Kaplan, D. L.; Tsukruk, V. V. Unfolding the Multi-length Scale Domain Structure of Silk Fibroin Protein. *Polymer* **2006**, *47*, 5821–5830.
- (64) Gupta, M. K.; Singamaneni, S.; McConney, M. M.; Drummy, L. F.; Naik, R. R.; Tsukruk, V. V. A Facile Fabrication Strategy for Patterning Protein Chain Conformation in Silk Materials. *Adv. Mater.* **2010**, *22*, 115.
- (65) Gopinadham, M.; Ivanova, O.; Ahrens, H.; Guenther, J. U.; Steitz, R.; Helm, C. A. The Influence of Secondary Interactions During the Formation of Polyelectrolyte Multilayers: Layer Thickness, Bound Water and Layer Interpenetration. *J. Phys. Chem. B* **2007**, *111*, 8426.
- (66) Losche, M.; Schmitt, J.; Decher, G.; Bouwman, W. G.; Kjaer, K. Detailed Structure of Molecularly Thin Polyelectrolyte Multilayer Films on Solid Substrates as Revealed by Neutron Reflectometry. *Macromolecules* **1998**, *31*, 8893.
- (67) Haas, H.; Steitz, R.; Fasano, A.; Liuzzi, G. M.; Polverini, E.; Cavatorta, P.; Riccio, P. Laminar Order within Langmuir-Blodgett Multilayers from Phospholipid and Myelin Basic Protein: A Neutron Reflectivity Study. *Langmuir* **2007**, *23*, 8491.
- (68) Wang, X.; Kim, H. J.; Xu, P.; Matsumoto, A.; Kaplan, D. L. Biomaterial Coatings by Stepwise Deposition of Silk Fibroin. *Langmuir* **2005**, *21*, 11335.
- (69) Shulha, H.; Foo, C. W. P.; Kaplan, D. L.; Tsukruk, V. V. Unfolding the Multi-length Scale Domain Structure of Silk Fibroin Protein. *Polymer* **2006**, *47*, 5821.

(70) Valluzzi, R.; Winkler, S.; Wilson, D.; Kaplan, D. L. Silk: Molecular Organization and Control of Assembly. *Philos. Trans. R. Soc. London B* **2002**, 357, 165.

(71) Bini, E.; Knight, D. P.; Kaplan, D. L. Mapping Domain Structures in Silks from Insects and Spiders Related to Protein Assembly. *J. Mol. Biol.* **2004**, 335, 27.

(72) Zhou, C.-Z.; Confalonieri, F.; Jacquet, M.; Perasso, R.; Li, Z.-G.; Janin, J. Silk Fibroin: Structural Implications of a Remarkable Amino Acid Sequence. *Proteins: Struct., Funct., Genet.* **2001**, 44, 119.

(73) Omenetto, F. G.; Kaplan, D. L. New Opportunities for an Ancient Material. *Science* **2010**, 329, 528.

(74) Kharlampieva, E.; Jung, C. M.; Kozlovskaya, V.; Tsukruk, V. V. Secondary Structure of Silaffin at Interfaces and Titania Formation. *J. Mater. Chem.* **2010**, 20, 5242.

(75) Cho, J.; Char, K.; Hong, J.-D.; Lee, K.-B. Fabrication of Highly Ordered Multilayer Films Using a Spin Self-assembly Method. *Adv. Mater.* **2001**, 13, 1076.

(76) Craig, V. S. J. Very Small Bubbles at Surfaces-the Nanobubble Puzzle. *Soft Matter* **2011**, 7, 40.

(77) Song, B.; Walczyk, W.; Schoher, H. Contact Angles of Surface Nanobubbles on Mixed Self-Assembled Monolayers. *Langmuir* **2011**, 27, 8223.

(78) Ochanda, F. O.; Samaha, M. A.; Tafreshi, H. V.; Tepper, G. C.; Gad-el-Hak, M. Salinity Effects on the Degree of Hydrophobicity and Longevity for Superhydrophobic Fibrous Coatings. *J. Appl. Polym. Sci.* **2012**, 124, 5021.